Inorganic Chemistry

Article

pubs.acs.org/IC

Combined MCD/DFT/TDDFT Study of the Electronic Structure of Axially Pyridine Coordinated Metallocorroles

Hannah M. Rhoda,[‡] Laura A. Crandall,[†] G. Richard Geier, III,[§] Christopher J. Ziegler,*[,†] and Victor N. Nemykin*[,‡]

[†]Department of Chemistry, University of Akron, 190 E. Buchtel Common, Akron, Ohio 44325-3601, United States

[‡]Department of Chemistry & Biochemistry, University of Minnesota Duluth, 1039 University Drive, Duluth, Minnesota 55812, United States

[§]Department of Chemistry, Colgate University, Hamilton, New York 13346, United States

Supporting Information

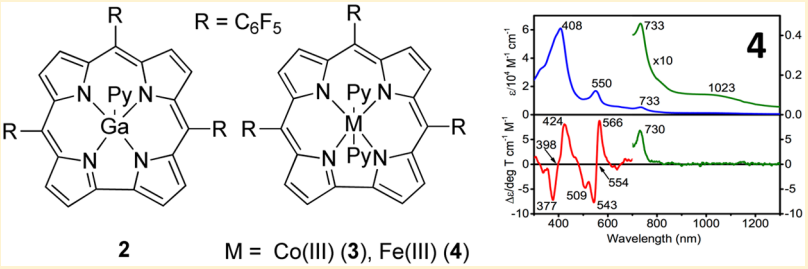

ABSTRACT: A series of metallocorroles were investigated by UV−vis and magnetic circular dichroism spectroscopies. The diamagnetic distorted square-pyramidal main-group corrole Ga(tpfc)py (**2**), the diamagnetic distorted octahedral transition-metal adduct Co(tpfc)$(py)_2$ (**3**), and paramagnetic distorted octahedral transition-metal complex Fe(tpfc)$(py)_2$ (**4**) [H_3tpfc = tris(perfluorophenyl)corrole] were studied to investigate similarities and differences in the electronic structure and spectroscopy of the closed- and open-shell metallocorroles. Similar to the free-base H_3tpfc (**1**), inspection of the MCD Faraday *B*-terms for all of the macrocycles presented in this report revealed that a ΔHOMO < ΔLUMO [ΔHOMO is the energy difference between two highest energy corrole-centered π-orbitals and ΔLUMO is the energy difference between two lowest energy corrole-centered π^*-orbitals originating from $M_L \pm 4$ and $M_L \pm 5$ pairs of perimeter] condition is present for each complex, which results in an unusual sign-reversed sequence for $\pi-\pi^*$ transitions in their MCD spectra. In addition, the MCD spectra of the cobalt and the iron complexes were also complicated by a number of charge-transfer states in the visible region. Iron complex **4** also exhibits a low-energy absorption in the NIR region (1023 nm). DFT and TDDFT calculations were used to elaborate the electronic structures and provide band assignments in UV−vis and MCD spectra of the metallocorroles. DFT and TDDFT calculations predict that the orientation of the axial pyridine ligand(s) has a very minor influence on the calculated electronic structures and absorption spectra in the target systems.

INTRODUCTION

First discovered in the 1960s,[1] the corrole macrocycle has continued to attract interest for a wide variety of applications due to its unique chemical and physical properties. Corrole (**1**, Figure 1) is a contracted analogue of porphyrin, composed of four pyrrollic subunits with three bridging meso-carbon positions, and a direct bipyrrole linkage. The synthesis and modification of free-base corroles has been an active area of research.[2] The omission of one carbon atom from the macrocyclic backbone results in a number of structural changes in corrole relative to porphyrin, including a contracted metal binding core and three ionizable NH groups. Although modified from normal porphyrin, corrole retains an aromatic 18-electron annulene ring structure. Accordingly, the UV−vis spectrum has absorption similar to normal porphyrins, with Soret and Q-band features that can be described using Gouterman's four orbital model.[3,4] However, the electronic and spectroscopic properties of corrole have features that are notably altered from normal porphryins. With free-base corroles, such differences include solvent-dependent absorption and emission behavior as well as increased quantum yields of fluorescence.[5]

The metal binding chemistry of corrole has also been an area of intense investigation, and the metal complexes of corrole have been used as catalysts,[6] sensors,[7] and heme model complexes.[8] The contracted core and trianionic character of the macrocycle affect how metal ions bind to corrole, especially with regard to stabilizing high-valent oxidation states. Thus, oxidation states +3 and above are typically observed in corroles. Corroles can bind transition-metal and main-group ions from across the periodic table, and much work has been carried out

Received: December 9, 2014
Published: May 7, 2015

DOI: 10.1021/ic502946t
Inorg. Chem. 2015, 54, 4652−4662

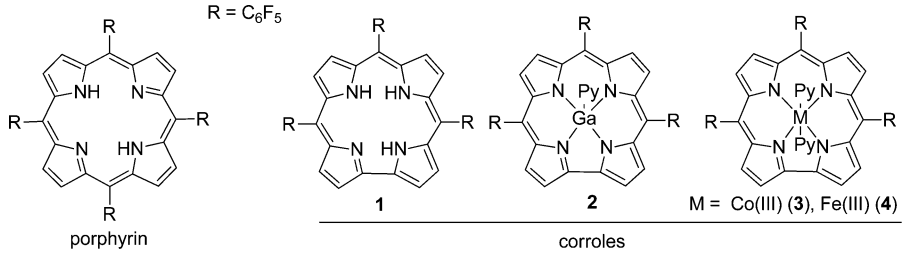

Figure 1. Structures of corroles **1**–**4** and the reference porphyrin macrocycle.

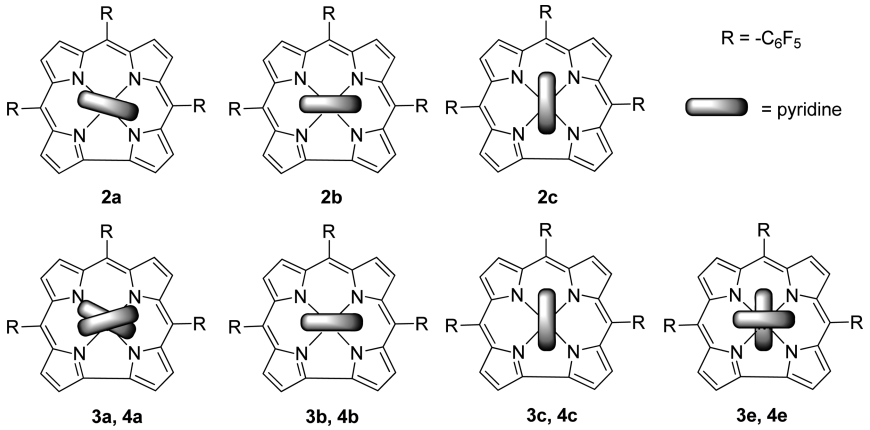

Figure 2. Structures of corroles **2**–**4** used in DFT and TDDFT calculations.

developing the metalation chemistry for this macrocycle. Nonetheless, much fundamental chemistry and properties of corrole and corrole metal complexes remain to be investigated.

To our surprise, the magnetic circular dichrosim (MCD) spectroscopy of the metallocorroles is completely unexplored despite the potential for MCD spectroscopy to provide accurate assignment of the optical transitions observed in such complexes. In this Article, we present the first study on the MCD spectra of a series of metallocorroles. Previously, we presented the first study of the MCD spectra of free-base corrole macrocycles.[9] Since our initial report, there has been one study on the MCD spectroscopy of a phosphorus corrole.[10] For the present study, we used the readily available tris-(pentafluorophenyl)corrole (**1**), which can be produced in decent yields,[2,11] and the free-base corrole has already been investigated by MCD spectroscopy.[9] We have collected MCD spectra from three different systems that reflect part of the diversity of the metal complexes for this porphyrinoid (Figure 1): a diamagnetic main-group distorted square-pyramidal metal corrole (Ga(III), **2**), a diamagnetic distorted octahedral transition-metal corrole (Co(III), **3**), and a paramagnetic distorted octahedral transition-metal corrole (Fe(III), **4**). All three complexes have a central metal ion in a +3 oxidation state and have an identical axial ligand(s) (pyridine). Compound **2** has one axial pyridine, whereas transition-metal complexes **3** and **4** have two pyridines bound to the metal ion. In all three metal adducts, we observe sign-reverse (positive-to-negative intensities in ascending energy) features in the Soret and Q-type band regions. This is the opposite trend as seen in normal porphyrins, but similar behavior was observed in free-base corroles[9] as well as the porphyrin isomer N-confused porphyrin.[12] This reverse behavior in the Faraday *B*-terms indicates that the magnitude of the splitting between the corrole-centered π^* LUMO and LUMO + 1 (originating from $M_L \pm 5$ pair of the perimeter) is greater than that seen for the corrole-centered π HOMO and HOMO − 1 (originating from $M_L \pm 4$ pair of the perimeter).[13] Additionally, using TDDFT methods, we were able to probe the degree of participation of the metal orbitals in the Gouterman-type frontier orbitals, which can provide insight into the noninnocent nature of the corrole ligand as well as the effects of d orbital occupancy on the UV–vis spectra of the corroles.

EXPERIMENTAL SECTION

Synthesis and Instrumentation. All solvents were purchased from commercial sources and dried using standard approaches prior to experiments. Free-base 5,10,15,25-pentafluorophenyl corrole (**1**) was synthesized as described previously.[2,5,11] The metal complexes **2**, **3**, and **4** were prepared from **1** using published methods.[14]

UV–vis–NIR data were obtained on a Jacso V-670 spectrometer in DCM, pyridine, or toluene as solvents. MCD data were recorded using an OLIS DCM 17 CD spectropolarimeter using a permanent 1.4 T DeSa magnet. The spectra were recorded twice for each sample, once with a parallel field and again with an antiparallel field, and their intensities were expressed by molar ellipticity per T.[15]

Computational Aspects. All DFT calculations were conducted using the Gaussian 09 software.[16] The starting geometries of the corrole compounds were adopted from the experimental X-ray data; these were optimized at the DFT level using the TPSSh exchange-correlation functional (10% of Hartree–Fock exchange).[17] In the case of gallium corrole **2**, three different geometries were considered (Figure 2): (i) C_1 symmetry without any restrictions (**2a**); (ii) pyridine ligand is parallel to the short corrole C–C bond (C_s symmetry, **2b**); and (iii) pyridine ligand is perpendicular to the short corrole C–C bond (C_s symmetry, **2c**). In the case of cobalt (s = 0, **3**) and iron ($s = {}^1/_2$, **4**) corroles, four different geometries were considered: (i) C_1 symmetry without any restrictions (**3a** and **4a**); (ii) both pyridine ligands are parallel to the short corrole C–C bond (C_{2v} symmetry, **3b** and **4b**); (iii) both pyridine ligands are perpendicular to the short corrole C–C bond (C_{2v} symmetry, **3c** and **4c**); and (iv) one pyridine ligand perpendicular and one pyridine ligand parallel to the short corrole C–C bond (C_s symmetry, **3d** and **4d**). Equilibrium

DOI: 10.1021/ic502946t
Inorg. Chem. 2015, 54, 4652–4662

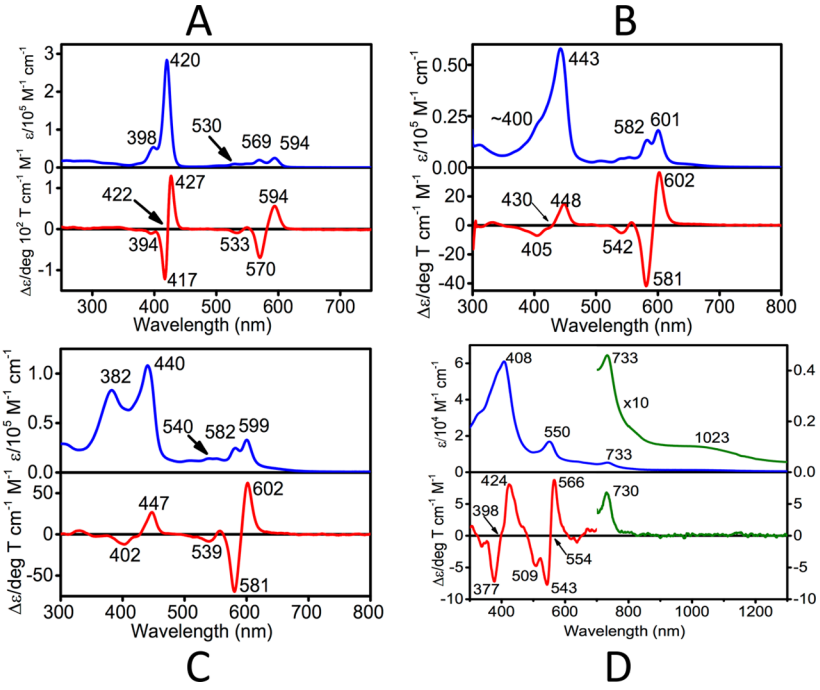

Figure 3. UV−vis and MCD spectra of compounds **2**−**4**. (A) Gallium corrole **2** in DCM with a drop of pyridine. (B) Cobalt corrole **3** in pyridine. (C) Cobalt corrole **3** in DCM. (D) Iron corrole **4** in toluene with a drop of pyridine.

geometries were confirmed by frequency calculations and specifically by the absence of imaginary frequencies. The Wachter's full-electron basis set[18] was utilized for the gallium, cobalt, and iron atoms, while all other atoms were modeled using the 6-31G(d) basis set.[19] For the DFT and TDDFT calculations, solvent effects were calculated using the PCM approach[20] with DCM as a solvent. In the TDDFT calculations, the first 60 states were calculated for the cobalt corroles, and the first 40 and 80 states were calculated for the gallium and iron corroles, respectively. Molecular orbital contributions were compiled from single-point calculations using the QMForge program.[21]

RESULTS AND DISCUSSION

UV−Vis and MCD Spectra. The corrole macrocycle can readily bind metal ions, and M(III) complexes are typical for this ligand.[14] The Ga(III) adduct **2** can be produced via reaction of $GaCl_3$ with the free-base **1** in pyridine, resulting in a five coordinate complex with a single axial pyridine ligand. The transition-metal complexes **3** and **4** are prepared by reaction of $Co(OAc)_2{\cdot}4H_2O$ and $FeCl_2$, respectively, with free-base **1** followed by recrystallization in the presence of pyridine. Compounds **3** and **4** have nearly identical structures, with equatorial corrole coordination and two axial pyridines comprising the six coordinate metal ion coordination spheres. As a result of structural similarities for all three metal adducts, we can directly compare the effect of the identity and spin state of the metal ions on the spectroscopy of corrole.

In our previous work,[9] we investigated the MCD spectra of free-base corroles and were able to deduce from our measurements the relative energy levels and gaps between the frontier orbitals of the 18-electron annulene ring system. The MCD spectra of all so far studied free-base corroles exhibit what has been considered as unusual sign-reverse (positive-to-negative intensities in ascending energy) features in the Soret and Q-type band regions[9] similar to those seen in N-confused porphyrin[12] and in a small number of other porphyrinoids.[22] The sign-reverse features, as supported by our calculations, are consistent with an unusual ΔHOMO < ΔLUMO relationship between the π and π^* MOs in the corrole ring. The UV−vis spectra, MCD spectra, and emission spectra of free-base corroles are highly solvent dependent, we have investigated and discussed this aspect of corrole chemistry.[5,9] This solvent dependence is no longer observed upon metalation due to the loss of the internal protons, possible hydrogen bonding with the corrole, as well as variable tautomerization states.[9]

The UV−vis and MCD spectra of the three metal complexes of free-base corrole **1** are shown in Figure 3. The gallium corrole **2** exhibits an absorption spectrum with an intense Soret band (420 nm) and three lower intensities Q-type bands at 530, 569, and 594 nm (Figure 1A). The increase in intensity observed in the Q-band region is similar to that seen in chlorins and in the external tautomer of N-confused porphyrin.[23,24] However, the spectrum of **2** is also very similar to that observed in normal Ga(TPP)Cl both in the energies and relative intensities of the transitions and in the number of Q bands.[25] The MCD spectrum of corrole **2** exhibits four strong Faraday *B*-terms in the 250−700 nm range. A positive Faraday *B*-term at 594 nm and a negative MCD *B*-term at 570 nm correlate well with 594 and 569 nm bands observed in the UV−vis spectrum of complex **2**. The Soret band region in the MCD spectrum of complex **2** is dominated by positive and negative MCD *B*-terms observed at 427 and 417 nm. These two *B*-terms form a MCD pseudo-*A*-term centered at 422 nm, which is close to the observed Soret band (420 nm) in the UV−vis spectrum of complex **2**. The positive-to-negative (in ascending energy) sequence of the Faraday *B*-terms in complex **2** is clearly indicative of a situation when ΔHOMO < ΔLUMO [ΔHOMO is the energy difference between two highest energy corrole-centered π-orbitals, and ΔLUMO is the energy difference between two lowest energy corrole-centered π^*-orbitals].[13] In the analogous phosphorus complex of a carboxymethylphenyl corrole studied by Kobayashi and co-workers, a similar positive to negative Faraday *B*-term behavior was observed.[10] In the phosphorus corrole and in compound **2**, the decrease in

DOI: 10.1021/ic502946t
Inorg. Chem. 2015, 54, 4652−4662

symmetry in the macrocycle backbone removes the degeneracy of the corrole-centered LUMO and LUMO + 2, and splits them to a greater degree than the corrole-centered HOMO and HOMO − 1 levels.

For the cobalt complex of corrole (compound **3**), Gross and co-workers reported that the six coordinate complex exists in equilibrium with a five coordinate complex at low concentrations of pyridine.[26] Earlier, Murakami and co-workers reported that, for the octaalkyl cobalt corroles, low pyridine concentration resulted in aggregation and that dimerization could occur in the Co(II) analogues.[27] We also observed different spectra for **3** in dichloromethane versus pure pyridine (Figure 1B,C). In the case of pure pyridine solution, UV−vis and MCD spectra of the low-spin cobalt(III) complex **3** look quite similar to those of gallium analogue **2**, except the complex **3** has lower energies of Q- and B-bands as well as larger bandwidths. Specifically, the Q-band region of the MCD spectrum of **3** is dominated by a positive Faraday *B*-term at 602 nm and a negative Faraday *B*-term at 581 nm, which correlate well with UV−vis bands at 601 and 582 nm, respectively. Similarly, a positive Faraday *B*-term at 448 nm and a negative *B*-term at 405 nm dominate the Soret band region of MCD spectrum of complex **3**, which correlate with the most intense absorption band of **3** observed in the UV−vis spectrum. It is interesting to note, however, that, in the case of cobalt corrole **3**, the MCD *B*-terms are more intense in the Q-band region, while in gallium corrole **2** they are more intense in the Soret band region. As in the gallium corrole **2**, we observe strong positive to negative Faraday *B*-terms, which as before indicates a ΔHOMO < ΔLUMO configuration in **3**. The UV−vis and MCD spectra of complex **3** in pure DCM are different from those observed in pyridine (Figure 1C). Although the Q-band regions in pyridine and DCM are almost identical, an additional strong absorption band at 382 nm has been observed in UV−vis spectrum of complex **3** in DCM. This new band is associated with a quite weak MCD signature, which could be consistent either with formation of H-type cofacial dimer similar to those observed in the main-group and transition-metal phthalocyanines[28] or with dissociation of one axial pyridine ligand with formation of the pentacoordinated cobalt corrole complex **3**. In the latter case, the new weak MCD band can be associated with charge-transfer transitions, which are absent in the hexacoordinated corrole **3**. Gross and co-workers[6a,d,e] discussed equilibrium between penta- and hexacoordinated cobalt corroles as a function of solvent. We also have seen a clear disappearance of the band at 382 nm in UV−vis spectrum of cobalt corrole **3** upon titration of DCM solution with pyridine (Figure 4). Moreover, excellent agreement between TDDFT-predicted for pentacoordinated cobalt corrole **3** and the experimental spectrum of this compound in DCM as well as the absence of aggregate peaks in APCI and ESI mass spectra of corrole **3** allowed us to suggest an axial ligand dissociation as the main reason for observable UV−vis and MCD spectra in DCM. Our proposed reaction chemistry that describes this pyridine-dependent behavior is shown in Scheme 1. In order for such dimerization to occur in the bis(axially) coordinated complex **3**, one of the axial pyridine ligands should dissociate. Although mechanistically, such axial ligand dissociation is trivial, complex **3** is formally a d^6 system, which should be kinetically very inert.[29] Axial ligand dissociation in complex **3** will be explained below on the basis of DFT calculations.

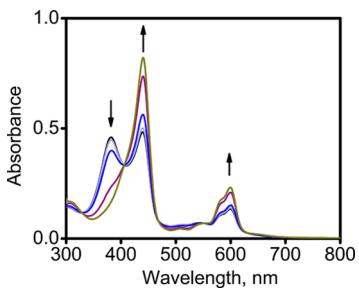

Figure 4. Transformation of the UV−vis spectrum of cobalt corrole **3** in DCM upon stepwise addition (0−10 μL) of pyridine.

The UV−vis and MCD spectra of iron complex **4** in pyridine/toluene mixture are strikingly different from those of free-base corroles, the main-group corrole **2**, or even the diamagnetic transition-metal corrole **3**. Gross and co-workers reported that complex **4** exhibits NMR and EPR features that correspond to a low-spin ($s = {}^1/_2$) Fe(III) metal complex, which is expected for the relatively strong ligand field environment of the trianionic corrole macrocycle and axial pyridines.[26] The features in the UV−vis spectrum are rather broad, with a Soret-type absorption centered at 408 nm, and Q-band features at 550 and 733 nm. We also observed a very low-energy absorption in the near-infrared (NIR) region around 1023 nm, which can be seen in Figure 1D. The same region in the cobalt complex **3** shows no such absorption in the NIR region. However, Fe(III) porphyrins do exhibit low-energy ligand to metal charge-transfer (LMCT) bands resulting from low-spin ($s = {}^1/_2$) configurations.[30] The MCD spectrum exhibits features consistent with the UV−vis spectrum of complex **4**. Indeed, the Soret-type band in MCD spectrum of complex **4** is represented by positive (424 nm) and negative (377 nm) signals centered at 398 nm. The intensity of this feature is close to the intensity of another pseudo-*C*-term, which is centered at 554 nm and consists of positive (566 nm) and negative (543 nm) *B*-term components. It is interesting to note that the relatively weak but easily detectable positive Faraday *B*-term at 730 nm in MCD spectrum of **4** can be clearly associated with the 733 nm band in its UV−vis spectrum, while no clear MCD signal was observed for the 1023 nm band at room temperature even at high concentrations of sample.

DFT and TDDFT Calculations. To obtain insight into the electronic structures of corroles **2**−**4** and to interpret their observed UV−vis and MCD spectra, we conducted DFT and TDDFT calculations on these systems. In general, the metal complexes of corrole have received much attention from a computational standpoint as a result of their unique reactivities and the observed "noninnocence" of the macrocycle.[31] In particular, calculations have focused on understanding the relationship between the corrole macrocycle and stabilization of the central metal high-valent oxidation states.[31] Several research groups presented DFT calculations on gallium,[32] cobalt(III),[33] and iron(III)[34] corroles, but in many of those calculations pyridine axial ligands were not considered. Although truncation of the axial pyridine ligand can be (to some extent) justified for gallium corrole, axial pyridine ligands should be always considered in the case of cobalt(III) and iron(III) corroles as they directly influence spin state and the energies of the charge-transfer transitions. Having this consideration in mind, we conducted DFT calculations including the geometries of the axial pyridine ligand(s). In all cases, DFT-predicted geometries are in good agreement with known X-ray crystal structures for

DOI: 10.1021/ic502946t
Inorg. Chem. 2015, 54, 4652−4662

Scheme 1. Proposed Transformation of the Hexacoordinated Cobalt Corrole 3 into a Pentacoordinated Form

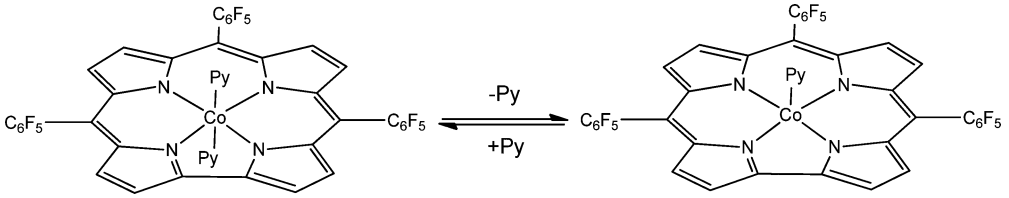

Ga(III) and Fe(III) corroles (Supporting Information Table 1).[35] As discussed below, DFT predicts only small energy differences for different orientations of the axial pyridine ligand(s) thus confirming a small rotational barrier for this group. Because of such a small rotational barrier, however, one cannot consider only crystallographically observed geometries, as in solution axial ligand(s) can adopt a variety of orientations. More important, different orientations of the axial pyridine ligand(s) in transition-metal corroles **3** and **4** can easily change the degree of interaction with the metal-centered d-manifold, thus changing energies and compositions of the metal-centered MOs. For these reasons all specific orientations of the pyridine ligand(s) in target corroles are discussed below.

There are also two recent TDDFT calculations on the $\pi-\pi^*$ transition energies in metal-free[9] and phosphorus-containing[10] corroles. Indeed, we recently presented TDDFT calculations on a series of meso-substituted free-base corroles, and noted a correlation between the ΔLUMO and ΔHOMO and the sign-reverse features observed in the MCD spectra.[9] The TDDFT calculations that are most relevant to the current work were presented recently by Kobayashi and co-workers on the oxyphosphorous 5,10,15-tris(*p*-methoxycarbonylphenyl)corrole system.[10] In this report, the unsubstituted phosphorus(V) macrocycle along with the tris(phenyl) and tris (*p*-methoxycarbonylphenyl) substituted variants were studied. In each case, the same trends were observed as seen in the free-base corroles. The ΔLUMO remains larger than the ΔHOMO (resulting in the reverse sign Faraday *B*-terms in the corresponding MCD spectra), but the presence of the phenyl rings and ester functional groups does increase the ΔHOMO, although not enough to alter the reverse sign Faraday *B*-term.

Because of the presence of the closed-shell main-group metal ion, it is expected that the electronic structure and properties of the excited states in complex **2** would be the easiest to analyze. Molecular orbital energies for complex **2** with different orientations of the axial pyridine ligand are shown in Figure 5; their profiles are pictures in Figures 6 and Supporting Information Figure 1, while orbital compositions are listed in Supporting Information Table 1. For compound **2**, as a complex with a closed-shell main-group metal ion, Ga(III), we expected minimal perturbation caused by the axial pyridine position to the frontier orbital energies and compositions. Geometry optimization without any symmetry restraints results in axial ligand orientation very close to the parallel with respect to the corrole C−C bond (Figure 6). The energy difference between this and the idealized C_s geometry is virtually zero, while the energy of the idealized geometry with the axial pyridine ligand perpendicular to the corrole C−C bond is slightly (0.34 kcal/mol) higher. As we had surmised, there is little metal orbital involvement in the frontier orbitals of compound **2** (Supporting Information Table 2). The natures of the HOMO and HOMO − 1 are very similar for all orientations and correlate well with the previous DFT

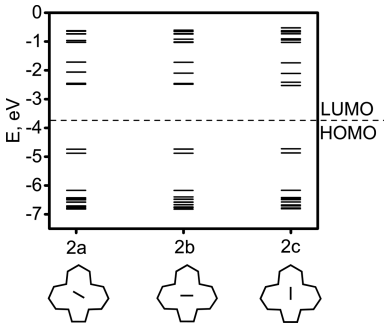

Figure 5. Frontier orbitals energy diagram for gallium corrole **2** predicted at the DFT level. The diagrams at the bottom of the chart show the orientations of the pyridine ring with regard to the macrocycle.

calculations.[31] In particular, the HOMO is dominated by the contributions from the nitrogen atoms, meso-carbon atoms, and the short corrole C−C bonds (Figure 6). Although not identical (because of the lack of one meso-carbon), the HOMO resembles, to some extent, Gouterman's a_{2u} type orbital.[4] Similarly, pyrrolic α- and β-carbon atoms are predominant contributors into the HOMO − 1 (Figure 6), which resembles, to some extent, Gouterman's a_{1u} type orbital.[4] For the symmetry with parallel pyridine ligand, the LUMO and LUMO + 1 both exhibit significant amounts of pyridine ligand character. For the C_1 and the C_s symmetries with a pyridine ligand parallel to the corrole C−C bond (**2a** and **2b**), the LUMO and LUMO + 2 have π^* character and are dominated by contribution from the corrole core, while the LUMO + 1 is primarily pyridine in character. In the case of the perpendicular orientation of the axial pyridine ligand (**2c**), both LUMOs have a large contribution, while LUMO + 1 is dominated by the contribution of the axial pyridine ligand (Supporting Information Table 2). The LUMO + 2 remains a purely corrole-centered orbital. Overall, DFT calculations on complex **2** reveal that the corrole-based ΔLUMO (not including the predominantly pyridine-based LUMO + 1) is larger (0.385−0.423 eV) than the ΔHOMO (0.142−0.146 eV), which is in agreement with the reverse sign Faraday *B*-term observation in its MCD spectrum.

In the case of diamagnetic low-spin cobalt corrole **3**, both axial pyridine ligands were used in DFT calculations to mimic an actual ligand field environment around a cobalt center. Once again, we calculated four different structures based on the orientations of the pyridine rings: a C_1 symmetry, **3a**, with no geometric restrictions, a C_{2v} symmetry with both pyridine ligands parallel to the short corrole C−C bond (**3b**), a C_{2v} symmetry with the pyridines perpendicular to the short corrole C−C bond (**3c**), and an intermediate C_s symmetry with the pyridine ligands in orthogonal orientations (**3d**). The relative orbital energies for **3a**−**d** based on their symmetries are shown in Figure 7. The relative energies of **3a**−**c** are very close to each

DOI: 10.1021/ic502946t
Inorg. Chem. 2015, 54, 4652−4662

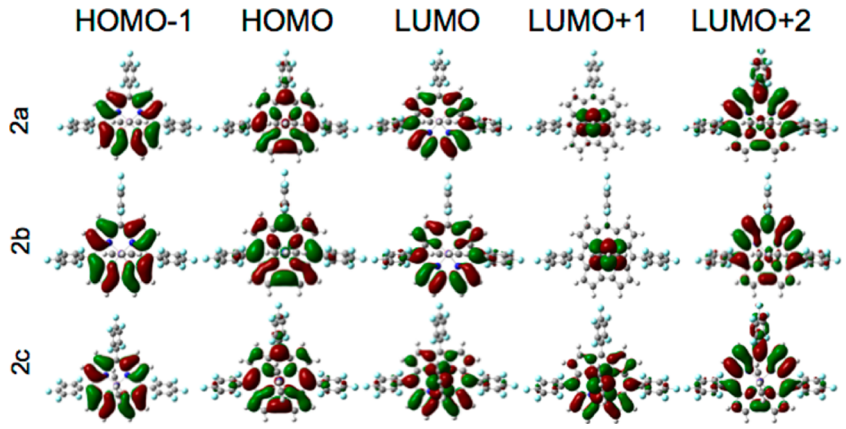

Figure 6. Frontier orbitals for gallium corrole **2** predicted at the DFT level for different orientations of the axial pyridine ligand.

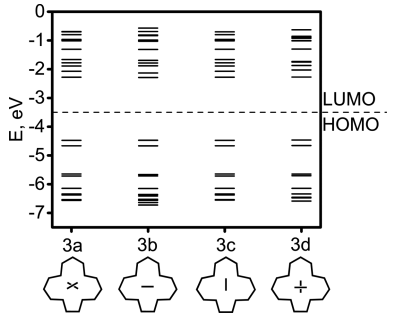

Figure 7. Frontier orbital energy diagram for cobalt corrole **3** predicted at the DFT level. The diagrams at the bottom of the chart show the orientations of the pyridine rings with regard to the macrocycle.

other, while the energy difference between **3a** and **3d** is 2.61 kcal/mol. In all cases, the HOMO and HOMO − 1 are similar to those observed in gallium corrole **2** (Figure 8). Indeed, nitrogen atoms contribute ∼25% into the HOMO, while *α*- and *β*-pyrrolic carbons contribute the most into the HOMO − 1 (Supporting Information Table 3). Unlike in gallium analogue **2**, cobalt d_{xz} and d_{yz} orbitals have a large contribution into the HOMO − 2 and HOMO − 3. Again, similar to the gallium complex **2**, the LUMO and the LUMO + 2 are predominantly corrole-centered π^* orbitals, which are used in our ΔLUMO calculations. The LUMO + 1 in cobalt corroles **3a**−**d** has almost equivalent contributions from the cobalt d_{z^2} orbital and two pyridine axial ligands (Supporting Information Table 3, Figure 8, and Supporting Information Figure 2). Once again, our calculations indicate that the ΔLUMO (0.391−0.406 eV) > ΔHOMO (0.191−0.195 eV) condition occurs in **3**, producing the observed MCD Faraday *B*-term sequence.

Cobalt(III) corrole complex **3** is formally a d^6 system, which is well-known to be kinetically very stable toward the dissociation of ligands.[29] Previous[26,27] and current data on this complex, however, are clearly suggestive of the presence of a non-negligible $L_2Co(tpfc) \rightleftarrows LCo(tpfc) + L$ axial ligand dissociation process in solution. Such axial ligand dissociation can be at least partially explained by the possible presence of a valence isomer in **3**. Indeed, taking into consideration noninnocent redox properties of the corrole ligand, one might expect the presence of two resonance structures for complex **3**: $L_2Co^{III}(tpfc^{3-}) \leftrightarrow L_2Co^{II}(tpfc^{2-})$. The latter formally has a d^7 configuration, and would exhibit much higher kinetic mobility of the axial ligand. In order to test such a possibility, we conducted a single-point calculation on the

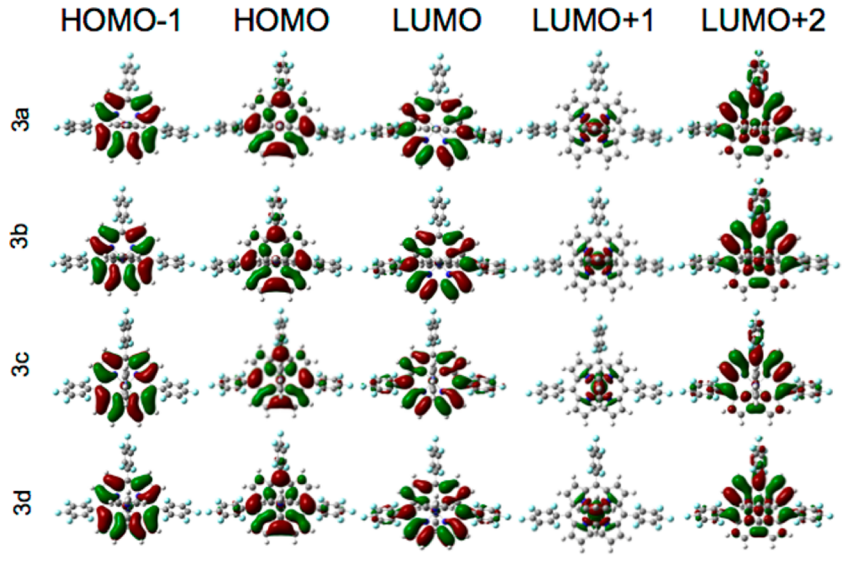

Figure 8. Frontier orbitals for cobalt corrole **3** predicted at the DFT level for different orientations of the two axial pyridine ligands.

DOI: 10.1021/ic502946t
Inorg. Chem. 2015, 54, 4652−4662

$L_2Co^{II}(tpfc^{2-})$ valence isomer using broken-symmetry calculation approach in which a low-spin ($s = {}^1/_2$) cobalt(II) center is antiferromagnetically coupled to the one-electron oxidized corrole ligand. Broken-symmetry calculations resulted in significantly higher energy (~71 kcal/mol) for the $L_2Co^{II}(tpfc^{2-})$ valence isomer. Moreover, optimization of the resulting wave function leads to its convergence to the $L_2Co^{III}(tpfc^{3-})$ valence isomer. Although calculated energy differences are expected to have a strong exchange-correlation functional dependence, it seems that the $L_2Co^{III}(tpfc^{3-})$ valence isomer is the only one present in solution, and the question of the increased lability of the axial ligand remains unclear.

For the pentacoordinated cobalt corrole complex, we calculated three different structures based on the orientations of the pyridine rings: a C_1 symmetry, **3e**, with no geometric restrictions, a C_s symmetry with both pyridine ligands parallel to the short corrole C−C bond (**3f**), and a C_s symmetry with the pyridines perpendicular to the short corrole C−C bond (**3g**). During geometry optimization, the C_1 geometry (**3e**) converged close to the C_s symmetry observed for **3f**. The relative orbital energies for **3e**,**f** based on their symmetries are shown in Figure 9. The relative energies of **3e**,**f** are close to each other with the largest energy difference between **3e** and **3f** being 0.4 kcal/mol. In all cases, the HOMO and HOMO − 1 are corrole-centered π-orbitals followed by HOMO − 2 and HOMO − 3 with a significant contribution from the cobalt d_{xz} and d_{yz} orbital corrole nitrogen atoms (Supporting Information Table 3, Figure 10). The major consequence of the axial ligand dissociation from the hexacoordinated cobalt corrole is a strong stabilization of the unoccupied cobalt d_{z^2} orbital. As a result of such stabilization, the LUMO in pentacoordinated corrole **3** is dominated by the cobalt d_{z^2} (~44%) and pyridine π^* (~24%) contributions. The LUMO + 1 and the LUMO + 3 are predominantly corrole-centered π^* orbitals, which are used in our ΔLUMO calculations. The LUMO + 2 is predicted to be an almost pure pyridine centered π^* orbital (Supporting Information Table 4, Figure 10, and Supporting Information Figure 3). Once again our calculations indicate that the ΔLUMO (0.381−0.393 eV) > ΔHOMO (0.107−0.117 eV) condition occurs in pentacoordinated **3e**−**g**, producing the observed MCD Faraday *B*-terms sequence.

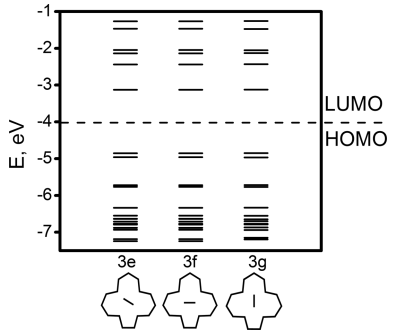

Figure 9. Frontier orbitals energy diagram for pentacoordinated cobalt corrole **3** predicted at the DFT level. The diagrams at the bottom of the chart show the orientations of the pyridine ring with regard to the macrocycle.

For the paramagnetic iron corrole **4**, which is isostructural to the bis-pyridine form of cobalt corrole **3**, we used the same set of the axial pyridine ligand arrangements. Again, the relative energies of **4a**−**c** are very close to each other, while the energy difference between **4a** and **4d** is 2.01 kcal/mol. The energy diagram of the open-shell molecular orbitals is shown in Figure 11; the relative contributions to the orbitals are shown in Supporting Information Table 5, and their profiles are presented in Figure 12 and in Supporting Information Figure 4. In all geometries of the pyridine ligands, unpaired electron density was found on the central iron atom (Supporting Information Table 5). The α-set of MOs in iron complex **4** is very close to DFT-predicted MOs in gallium and cobalt corroles **2** and **3**. Indeed, the HOMO resembles Gouterman's a_{2u} type orbital with substantial contribution from the nitrogen atoms, meso-carbon atoms, and the direct pyrrole−pyrrole

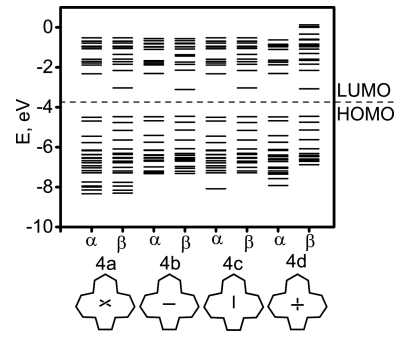

Figure 11. Frontier orbital energy diagram for iron corrole **4** predicted at the DFT level. The diagrams at the bottom of the chart show the orientations of the pyridine rings with regard to the macrocycle.

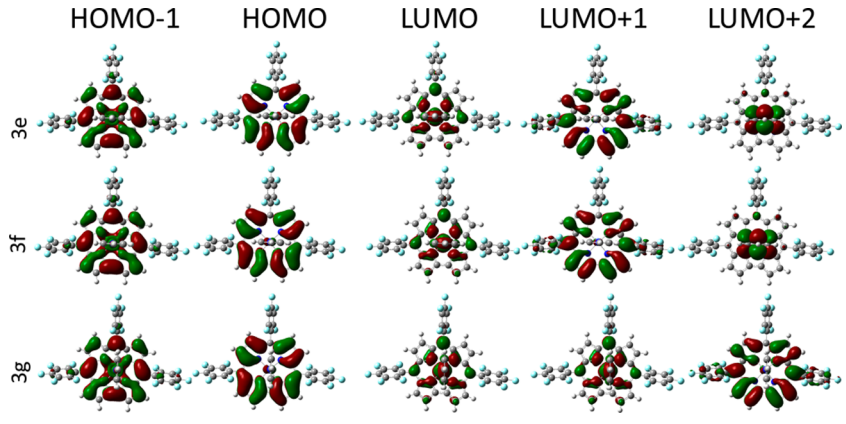

Figure 10. Frontier orbitals for pentacoordinated cobalt corrole **3** predicted at the DFT level for different orientations of the axial pyridine ligand.

DOI: 10.1021/ic502946t
Inorg. Chem. 2015, 54, 4652−4662

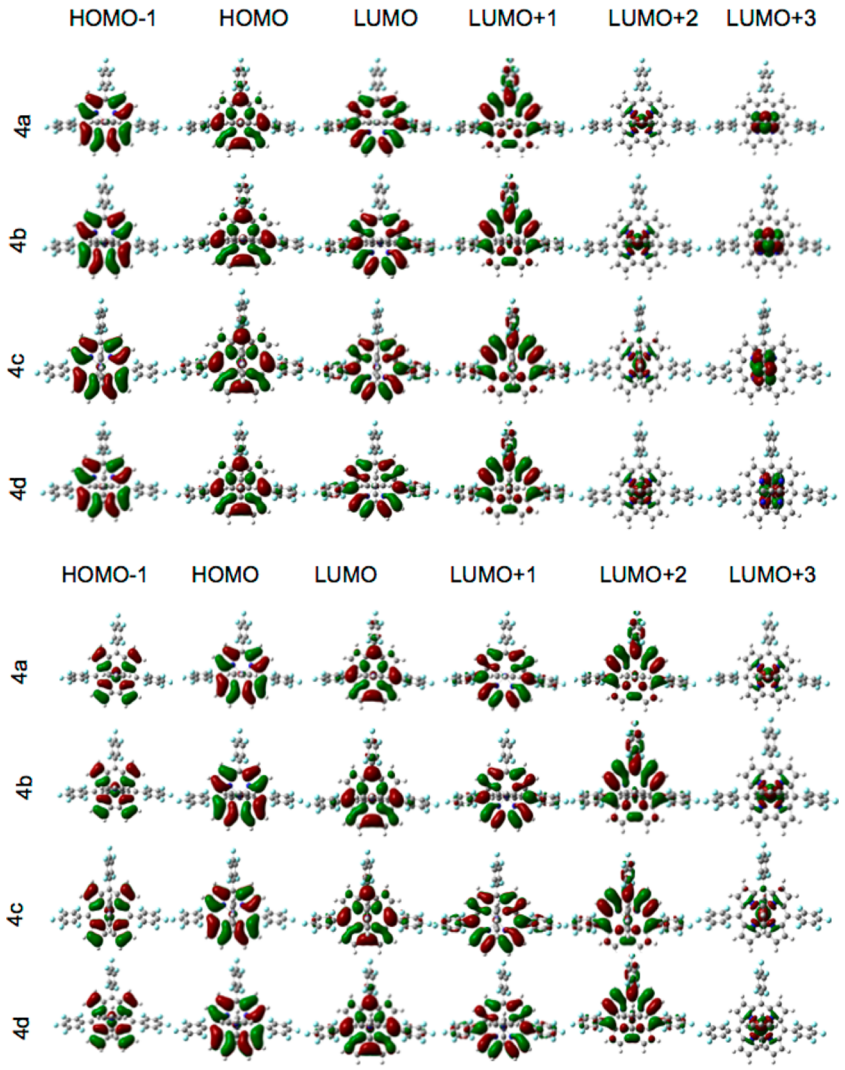

Figure 12. Frontier orbitals (top, α-set; bottom, β-set) for iron corrole **4** predicted at the DFT level for different orientations of the two axial pyridine ligands.

bond, while the HOMO − 1 is dominated by contribution from pyrrolic α- and β-carbons and resembles Gouterman's a_{1u} MO. In addition, HOMO − 2 and HOMO − 3 have significant iron d_{xz} and d_{yz} character, while HOMO − 4 is predominantly an iron-centered d_{xy} orbital. The LUMO and LUMO + 1 are similar to the LUMO and LUMO + 2 in gallium and cobalt complexes **2** and **3** and are corrole-core centered π^* MOs. In both α- and β-sets of MOs for **4a**−**d**, the pyridine π^* orbitals are of higher energy than the immediate (LUMO and LUMO + 1) frontier orbitals. This is in contrast with the gallium and cobalt corroles **2** and **3** in which pyridine π^* orbitals contribute significantly into the LUMO + 1. As expected, the LUMO in the β-set of MOs has significant iron character, and the overall spin densities for all possible axial pyridine ligands geometries **4a**−**d** are clearly suggestive of localization of the unpaired electron on iron center (Supporting Information Table 5). Again, in all cases **4a**−**d**, we observe a ΔLUMO (0.431−0.438 eV) > ΔHOMO (0.188−0.201 eV) relation that is in good agreement with the MCD experiments.

The electronic structure calculations on corroles **2**−**4** at the DFT level suggest two distinct cases. In the first case (gallium corrole **2**), no metal-centered orbitals were predicted in the frontier orbital region. Thus, it is expected that its UV−vis and MCD spectra could be entirely described by intense π−π^* transitions. Taking into account that the LUMO + 1 in corrole **2** is dominated by the axial pyridine ligand, expected π−π^* transitions could originate either from corrole-to-corrole or corrole-to-pyridine excitations. In the second case (corroles **3** and **4**), metal-centered MOs have significant contribution into the frontier orbital region. Thus, in addition to the above-mentioned π−π^* transitions, a set of metal-to-ligand and/or ligand-to-metal charge-transfer transitions are expected to appear in their UV−vis and MCD spectra. In order to correlate electronic structure of corroles **2**−**4** with the experimentally observed UV−vis and MCD spectra, we have conducted TDDFT calculations on all possible orientations of axial ligands in complexes **2**−**4**.

As expected, TDDFT-predicted UV−vis spectra of corrole **2** (Figure 13 and Supporting Information Figure 5) are dominated by π−π^* transitions, and predicted excited state energies are almost insensitive to the orientation of the axial pyridine ligand. In general, we observed excellent agreement between experimental and TDDFT-predicted UV−vis spectra of the gallium corrole **2** with the typical TDDFT errors at the ∼0.1 eV level. TDDFT predicts that the whole UV−vis spectrum of gallium corrole **2** can be described by the first six

DOI: 10.1021/ic502946t
Inorg. Chem. 2015, 54, 4652−4662

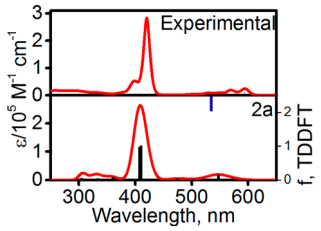

Figure 13. Experimental (top) and TDDFT-predicted values for gallium corrole **2a**. For TDDFT-predicted UV−vis spectra of **2** with different orientations of the axial pyridine ligand, see Supporting Information Figure 5. The energy of the second excited state of low-intensity is shown as a blue vertical bar.

excited states (Supporting Information Table 6). The Q-band region can be described by the first four low-intensity excited states. TDDFT predicts that the first two excited states are dominated by corrole-centered HOMO → LUMO and HOMO − 1 → LUMO transitions with a large contribution of the HOMO − 1 → LUMO + 1 and HOMO → LUMO + 1 single electron excitation, respectively. The energy differences between the first and the second excited states are in excellent agreement with the energy difference for the first two low-energy bands in UV−vis and MCD spectra of corrole **2**, although TDDFT-predicted intensity of the second band is underestimated. The third and fourth excited states in the visible range predominantly originate from the corrole-centered HOMO → LUMO + 2 and HOMO − 1 → LUMO + 2 transitions, respectively. TDDFT calculations predict that the Soret band region of corrole **2** originates from two excited states (states 5 and 6), which have high oscillator strengths. These two excited states have contributions from the HOMO → LUMO, HOMO − 1 → LUMO + 2, HOMO − 1 → LUMO + 2, HOMO → LUMO + 2, HOMO → LUMO + 1, and HOMO−1 → LUMO + 1 major excitations and are $\pi-\pi^*$ in nature.

In the case of the diamagnetic low-spin cobalt(III) corrole **3**, the LUMO + 1 orbital is close in energy to the LUMO and has ∼40% of cobalt ion and ∼40% of the axial pyridine ligands character. Thus, it could be expected that the single-electron excitations from the corrole-centered HOMO and HOMO − 1 to LUMO + 1 would result in formation of the low-energy excited states with significant LMCT character. Indeed, TDDFT calculations predict that the first two excited states in corrole **3** should be dominated by HOMO → LUMO + 1 (excited state 1, 598 nm) and HOMO − 1 → LUMO + 1 (excited state 2, 577 nm) single-electron transitions and thus, these excited states should have significant LMCT character (Figure 14, Supporting Information Figure 6 and Table 7). In addition, TDDFT-predicted excited state 5 (483 nm) and excited state 8 (464 nm) are dominated by the single-electron excitations to the LUMO + 1 and also have significant LMCT character. According to TDDFT calculations, all of these LMCT states, however, should have a low-intensity. TDDFT predicts that the Q-band region in UV−vis spectrum of corrole **3** should be dominated by the intense $\pi-\pi^*$ transition (excited state 3), which has the prominent corrole-core centered HOMO → LUMO character. This $\pi-\pi^*$ transition is closely followed by a less intense $\pi-\pi^*$ band originating from the HOMO → LUMO + 2 and HOMO − 1 → LUMO excitations. The energy difference between these two excited states is in good agreement with the energies and energy differences of two most intense bands experimentally observed in the Q-band region of complex **3**. In addition, four low-intensity bands at 481, 480, 448, and 447 nm with corrole-to-pyridine charge-transfer character were also predicted in the Q-band region of complex **3**. TDDFT predicts that most of the Soret band intensity in the UV−vis spectrum of corrole **3** should originate from two predominantly $\pi-\pi^*$ transitions (excited states 12 and 13), which have large contributions from single-electron excitations involving corrole-centered HOMO, HOMO − 1, LUMO, and LUMO + 2. The energies and intensities of these excited states have clear dependence on orientation of the axial ligands (Supporting Information Figure 6). The general agreement between TDDFT-predicted and experimental UV−vis spectra of corrole **3** is very good and explains a slightly broader absorption in UV and visible regions.

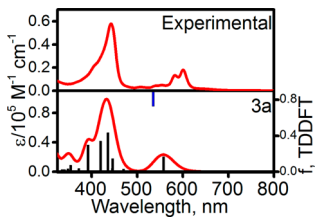

Figure 14. Experimental (top) and TDDFT-predicted values for hexacoordinated cobalt corrole **3a**. For TDDFT-predicted UV−vis spectra of **3** with different orientations of the axial pyridine ligand, see Supporting Information Figure 6. Energy of the second excited state of low-intensity is shown as a blue vertical bar.

In the case of pentacoordinate cobalt corrole **3**, TDDFT predicts four low-intensity LMCT transitions from predominantly corrole-centered π-orbitals to LUMO (excited states 1−4). According to our TDDFT calculations, two major transitions contribute in the visible region intensity (excited states 5 and 6), and are predominantly associated with corrole-centered $\pi-\pi^*$ single electron excitations from HOMO or HOMO − 1 to LUMO + 1 (Figure 15, Supporting Information Figure 7 and Table 8). Unlike in the hexacoordinate complex, both of these transitions have reasonable intensities and correlate well with two transitions observed in the visible region in DCM solution of corrole **3**. In addition, two other, almost independent of the axial ligand orientation, prominent absorption profiles were predicted by TDDFT in 400−450 and 350−380 nm regions (Figure 15, Supporting Information Figure 7 and Table 3). The first region is dominated by excited states 11 and 12, which are very similar in composition to those observed in the hexacoordinate cobalt analogue. The second region (350−380 nm) is dominated by several excited states (excited states 15, 20, 24, and 25), which mostly originate from

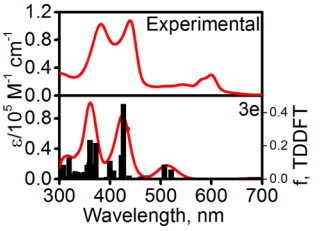

Figure 15. Experimental (top) and TDDFT-predicted values for pentacoordinated cobalt corrole **3e**. For TDDFT-predicted UV−vis spectra of **3e−g** with different orientations of the axial pyridine ligand, see Supporting Information Figure 7. Energies of the several important excited states of low-intensity are shown as blue vertical bars.

DOI: 10.1021/ic502946t
Inorg. Chem. 2015, 54, 4652−4662

the LMCT and MLCT single-electron transitions. This region is close to the experimentally observed additional band in the UV−vis spectrum of cobalt corrole **3** recorded in DCM, while its charge-transfer nature can explain the weak MCD signal associated with this experimental band.

The open-shell electronic structure of the iron corrole **4** allows low-energy transitions from corrole-centered MOs to the half-filled iron-centered orbital as well as low-energy transitions with significant d−d character. In agreement with these expectations, the first two excited states are predicted to have very low energies, near zero intensities, and significant d−d character (Figure 16, Supporting Information Figure 8 and Table 9). The first two nonzero intensity excited states predicted by TDDFT (excited states 3 and 4) were calculated close to the experimentally observed 1023 nm band and could be assigned to the transitions with significant LMCT character. Next, TDDFT-predicted two low-intensity excited states (excited states 6 and 7) with predominant $\pi-\pi^*$ character, which correlate well with the experimentally observed band at 733 nm. In addition, two more intense excited states 10 and 11 predicted by TDDFT at 553 and 546 nm also have predominant $\pi-\pi^*$ character and correlate very well with the experimentally observed band at 550 nm associated with positive and negative MCD *B*-terms at 566 and 543 nm, respectively. TDDFT predicts 36 excited states in the 415 and ∼2000 nm range, which correlate well with the general broad character of the UV−vis and rich character of the MCD spectra of corrole **4**. In the Soret band region of iron corrole **4**, TDDFT predicts two intense predominantly $\pi-\pi^*$ transitions calculated at 411 and 405 nm, which correlate well with UV−vis maximum at 408 nm. Similar to those for the hexacoordinated cobalt corrole **3**, TDDFT-predicted transitions in the Soret band region of iron(III) corrole **4** have only a small dependence on the axial ligand orientations (Supporting Information Figure 8). Overall correlation between experimental UV−vis spectrum of corrole **4** and TDDFT-predicted spectra of **4a**−**d** is excellent (Figure 16).

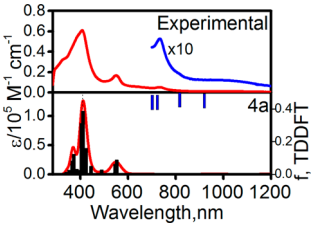

Figure 16. Experimental (top) and TDDFT-predicted for iron(III) corrole **4a**. For TDDFT-predicted UV−vis spectra of **4** with different orientations of the axial pyridine ligand, see Supporting Information Figure 8. Energies of the several important excited states of low-intensity are shown as blue vertical bars.

CONCLUSIONS

In our initial report on the magnetic circular dichroism of free-base corroles, we showed that these macrocycles exhibit both similarities and differences from normal free-base porphyrins. The metallocorroles exhibit similar similarities and differences as compared to the metalloporphyrins, and their electronic structures can be understood via Gouterman's four orbital model. Similar to the free-base H_3tpfc (**1**), inspection of the MCD Faraday *B*-terms for all of the macrocycles presented in this report revealed that the same ΔHOMO < ΔLUMO condition is present for each complex, which results in the sign-reversed sequence for $\pi-\pi^*$ transitions in their MCD spectra. In addition, the MCD spectra of the open d shell cobalt and the iron complexes **3** and **4** were also complicated by dynamics in solution and by the number of the charge-transfer states in visible region. For the cobalt complex **3**, we observed spectra that are dependent on the concentration of pyridine in solution; at low pyridine concentrations we hypothesize that both penta- and hexacoordinate cobalt corroles exist in solution. Additionally, the iron complex **4** exhibits a low-energy absorption in the NIR region (1023 nm) similar to those seen in Fe(III) porphyrin systems. DFT and TDDFT calculations were used to elaborate the electronic structures and provide band assignments in UV−vis and MCD spectra of metallocorroles. These calculations showed that there is a significant degree of d orbital involvement in the frontier orbitals for the open d shell corroles **3** and **4**. We are continuing our investigations into porphyrin and phthalocyanine analogues and the relationships between modifications to the macrocycle backbone and electronic structure.

ASSOCIATED CONTENT

Supporting Information

Coordinates for DFT optimized structures of **2**−**4**. Energies and expansion coefficients predicted by TDDFT for corroles **2**−**4**. Values predicted for all orientations by TDDFT and experimental and UV−vis spectra of corroles **2**−**4** in nm and cm^{-1} scale. The Supporting Information is available free of charge on the ACS Publications website at DOI: 10.1021/ic502946t.

AUTHOR INFORMATION

Corresponding Authors

*E-mail: ziegler@uakron.edu.
*E-mail: vnemykin@d.umn.edu.

Notes

The authors declare no competing financial interest.

ACKNOWLEDGMENTS

Generous support from the NSF CHE-1110455 and CHE-1401375, Minnesota Supercomputing Institute, and University of Minnesota Grant-in-Aid to V.N.N. is greatly appreciated.

REFERENCES

(1) (a) Johnson, A. W.; Kay, I. T. *Proc. Chem. Soc., London* **1964**, *89*, 211−214. (b) Johnson, A. W.; Kay, I. T. *J. Chem. Soc.* **1965**, 1620−1629. (c) Johnson, A. W.; Kay, I. T. *Proc. R. Soc. London, Ser. A* **1965**, *288*, 334−341.

(2) (a) Gross, Z.; Galili, N.; Saltsman, I. *Angew. Chem., Int. Ed.* **1999**, *38*, 1427−1429. (b) Gross, Z.; Galili, N.; Simkhovich, L.; Saltsman, I.; Botoshsnsky, M.; Blaser, D.; Boese, R.; Goldberg, I. *Org. Lett.* **1999**, *1*, 599−602. (c) Paolesse, R.; Jaquinod, L.; Nurco, D. J.; Mini, S.; Sagone, F.; Boschi, T.; Smith, K. M. *Chem. Commun.* **1999**, 1307−1308. (a) Geier, G. R., III; Chick, J. F. B.; Callinan, J. B.; Reid, C. G.; Auguscinski, W. P. *J. Org. Chem.* **2004**, *69*, 4159−4169. (b) Braaten, K. C.; Gordon, D. G.; Aphibal, M. M.; Geier, G. R., III. *Tetrahedron* **2008**, *64*, 9828−9836. (c) Koszarna, B.; Gryko, D. T. *J. Org. Chem.* **2006**, *71*, 3707−3717. (d) Gryko, D. T. *J. Porphyrins Phthalocyanines* **2008**, *12*, 906−917.

(3) (a) Ngo, T. H.; Puntoriero, F.; Nastasi, F.; Robeyns, K.; Van Meervelt, L.; Campagna, S.; Dehaen, W.; Maes, W. *Chem.—Eur. J.* **2010**, *16*, 5691−5705. (b) Tasior, M.; Gryko, D. T.; Pielacinska, D.; Zanelli, A.; Flamigni, L. *Chem.—Asian J.* **2010**, *5*, 130−140. (c) Tasior, M.; Gryko, D. T.; Cembor, M.; Jaworski, J. S.; Ventura, B.; Flamigni, L.

DOI: 10.1021/ic502946t
Inorg. Chem. 2015, 54, 4652−4662

New J. Chem. **2007**, *31*, 247−259. (d) Flamigni, L.; Ventura, B.; Tasior, M.; Gryko, D. T. *Inorg. Chim. Acta* **2007**, *360*, 803−813. (e) Ventura, B.; Esposti, A. D.; Koszarna, B.; Gryko, D. T.; Flamigni, L. *New J. Chem.* **2005**, *29*, 1559−1566. (f) Ding, T.; Aleman, E. A.; Modarelli, D. A.; Ziegler, C. J. *J. Phys. Chem. A* **2005**, *109*, 7411−7414. (g) Pomarico, G.; Vecchi, A.; Mandoj, F.; Bortolini, O.; Cicero, D. O.; Galloni, P.; Paolesse, R. *Chem. Commun.* **2014**, *50*, 4076−4078. (h) Vestfrid, J.; Goldberg, I.; Gross, Z. *Inorg. Chem.* **2014**, *53*, 10536−10542. (i) Santos, C. I. M.; Oliveira, E.; Barata, J. F. B.; Faustino, M. A. F.; Cavaleiro, J. A. S.; Neves, M. G. P. M. S.; Lodeiro, C. *Inorg. Chim. Acta* **2014**, *417*, 148−154.

(4) (a) Gouterman, M. *J. Mol. Spectrosc.* **1961**, *6*, 138−163. (b) Gouterman, M.; Wagnière, G. H.; Snyder, L. C. *J. Mol. Spectrosc.* **1963**, *11*, 108−127.

(5) Ding, T.; Harvey, J. D.; Ziegler, C. J. *J. Porphyrins Phthalocyanines* **2005**, *9*, 22−27.

(6) (a) Gross, Z.; Simkhovichm, L.; Galili, N. *Chem. Commun.* **1999**, 599−600. (b) Ramdhanie, B.; Telser, J.; Caneschi, A.; Zakharov, L. N.; Rheingold, A. L.; Goldberg, D. P. *J. Am. Chem. Soc.* **2004**, *126*, 2515−2525. (c) Collman, J. P.; Kaplum, M.; Decréau, R. A. *Dalton Trans.* **2006**, 554−559. (d) Aviv, I.; Gross, Z. *Synlett* **2006**, *6*, 951−953. (e) Simkhovich, L.; Gross, Z. *Tetrahedron Lett.* **2001**, *42*, 8089−8092. (f) Ou, Z.; Lu, A.; Meng, D.; Huang, S.; Fang, Y.; Lu, G.; Kadish, K. M. *Inorg. Chem.* **2012**, *51*, 8890−8896. (g) Chattopadhyay, P.; Matsuo, T.; Tsuji, T.; Ohbayashi, J.; Hayashi, T. *Organometallics* **2011**, *30*, 1869−1873. (h) Dogutan, D. K.; Stoian, S. A.; McGuire, R.; Schwalbe, M.; Teets, T. S.; Nocera, D. G. *J. Am. Chem. Soc.* **2011**, *133*, 131−140.

(7) (a) Mahammed, A.; Weaver, J. J.; Gray, H. B.; Abdelas, M.; Gross, Z. *Tetrahedron Lett.* **2003**, *44*, 2077−2079. (b) Li, C.-Y.; Zhang, X.-B.; Han, Z.-X.; Akermark, B.; Sun, L.; Shen, G.-L.; Yu, R.-Q. *Analyst* **2006**, *133*, 388−393. (c) Zhang, X.-B.; Han, Z.-X.; Fang, Z.-H.; Shen, G.-L.; Yu, R.-Q. *Anal. Chim. Acta* **2006**, *562*, 210−215. (d) Radecki, J.; Dehaen, W. *Comb. Chem. High Throughput Screening* **2006**, *9*, 399−406. (e) Radecki, J.; Stenka, I.; Dolusic, E.; Dehaen, W. *Electrochim. Acta* **2006**, *51*, 2282. (f) Yang, S.; Wo, Y.; Meyerhoff, M. E. *Anal. Chim. Acta* **2014**, *843*, 89−96.

(8) (a) Gross, Z. *J. Biol. Inorg. Chem.* **2001**, *6*, 733−738. (b) Goldberg, D. P. *Acc. Chem. Res.* **2007**, *40*, 626−634.

(9) Ziegler, C. J.; Sabin, J. R.; Geier, G. R., III; Nemykin, V. N. *Chem. Commun.* **2012**, *48*, 4743−4745.

(10) Liang, X.; Mack, J.; Zheng, L.-M.; Shen, Z.; Kobayashi, N. *Inorg. Chem.* **2014**, *53*, 2797−2802.

(11) (a) Wasbotten, I. H.; Wondimagegn, T.; Ghosh, A. *J. Am. Chem. Soc.* **2002**, *124*, 8104−8116. (b) Gryko, D. T.; Koszarna, B. *Org. Biomol. Chem.* **2003**, *1*, 350−357.

(12) (a) Sripothongnak, S.; Ziegler, C. J.; Dahlby, M. R.; Nemykin, V. N. *Inorg. Chem.* **2011**, *50*, 6902−6909. (b) Muranaka, A.; Homma, S.; Maeda, H.; Furuta, H.; Kobayashi, N. *Chem. Phys. Lett.* **2008**, *460*, 495−498.

(13) (a) Waluk, J.; Michl, J. *J. Org. Chem.* **1991**, *56*, 2729−2735. (b) Michl, J. *J. Am. Chem. Soc.* **1978**, *100*, 6801−6811. (c) Michl, J. *J. Am. Chem. Soc.* **1978**, *100*, 6812−6818.

(14) (a) Simkhovich, L.; Galili, N.; Saltsman, I.; Goldberg, I.; Gross, Z. *Inorg. Chem.* **2000**, *39*, 2704−2705. (b) Simkhovich, L.; Mahammed, A.; Goldberg, I.; Gross, Z. *Chem.—Eur. J.* **2001**, *7*, 1041−1055. (c) Bendix, J.; Dmochowski, I. J.; Gray, H. B.; Mahammed, A.; Simkhovich, L.; Gross, Z. *Angew. Chem., Int. Ed.* **2000**, *39*, 4048−4051.

(15) (a) Kobayashi, N.; Muranaka, A.; Mack, J. *Circular Dichroism and Magnetic Circular Dichroism Spectroscopy for Organic Chemists*; RSC: London, 2012; p 216. (b) Mason, W. R. *A Practical Guide to Magnetic Circular Dichroism Spectroscopy*; John Wiley & Sons, Inc.: Hoboken, NJ, 2007; p 223.

(16) Frisch, M. J.; Trucks, G. W.; Schlegel, H. B.; Scuseria, G. E.; Robb, M. A.; Cheeseman, J. R.; Scalmani, G.; Barone, V.; Mennucci, B.; Petersson, G. A.; Nakatsuji, H.; Caricato, M.; Li, X.; Hratchian, H. P.; Izmaylov, A. F.; Bloino, J.; Zheng, G.; Sonnenberg, J. L.; Hada, M.; Ehara, M.; Toyota, K.; Fukuda, R.; Hasegawa, J.; Ishida, M.; Nakajima, T.; Honda, Y.; Kitao, O.; Nakai, H.; Vreven, T.; Montgomery, J. A., Jr.; Peralta, J. E.; Ogliaro, F.; Bearpark, M.; Heyd, J. J.; Brothers, E.; Kudin, K. N.; Staroverov, V. N.; Kobayashi, R.; Normand, J.; Raghavachari, K.; Rendell, A.; Burant, J. C.; Iyengar, S. S.; Tomasi, J.; Cossi, M.; Rega, N.; Millam, N. J.; Klene, M.; Knox, J. E.; Cross, J. B.; Bakken, V.; Adamo, C.; Jaramillo, J.; Gomperts, R.; Stratmann, R. E.; Yazyev, O.; Austin, A. J.; Cammi, R.; Pomelli, C.; Ochterski, J. W.; Martin, R. L.; Morokuma, K.; Zakrzewski, V. G.; Voth, G. A.; Salvador, P.; Dannenberg, J. J.; Dapprich, S.; Daniels, A. D.; Farkas, Ö.; Foresman, J. B.; Ortiz, J. V.; Cioslowski, J.; Fox, D. J. *Gaussian 09, revision D.01*; Gaussian, Inc.: Wallingford, CT, 2009.

(17) Tao, J.; Perdew, J. P.; Staroverov, V. N.; Scuseria, G. E. *Phys. Rev. Lett.* **2003**, *91*, 146401−146405.

(18) Wachters, A. J. H. *J. Chem. Phys.* **1970**, *52*, 1033−1036.

(19) McLean, A. D.; Chandler, G. S. *J. Chem. Phys.* **1980**, *72*, 5639−5648.

(20) Tomasi, J.; Mennucci, B.; Cammi, R. *Chem. Rev.* **2005**, *105*, 2999−3093.

(21) Tenderholt, A. L. *QMForge, version 2.1*; Stanford University: Stanford, CA, 2011.

(22) (a) Mack, J.; Asano, Y.; Kobayashi, N.; Stillman, M. J. *J. Am. Chem. Soc.* **2005**, *127*, 17697−17711. (b) Mack, J.; Bunya, M.; Shimizu, Y.; Uoyama, H.; Komobuchi, N.; Okujima, T.; Uno, H.; Ito, S.; Stillman, M. J.; Ono, N.; Kobayashi, N. *Chem.—Eur. J.* **2008**, *14*, 5001−5020.

(23) (a) Wang, J.-J.; Liu, C.; Wu, J.; Liu, R.-R.; Zhang, P. *J. Heterocycl. Chem.* **2014**, *51*, 392−397. (b) Ogikubo, J.; Meehan, E.; Engle, J. T.; Ziegler, C. J.; Bruckner, C. *J. Org. Chem.* **2013**, *78*, 2840−2852. (c) Ryppa, C.; Niedzwiedzki, D.; Morozowich, N. L.; Srikanth, R.; Zeller, M.; Frank, H. A.; Bruckner, C. *Chem.—Eur. J.* **2009**, *15*, 5749−5762.

(24) Ziegler, C. J.; Erickson, N. R.; Dahlby, M. R.; Nemykin, V. N. *J. Phys. Chem. A* **2013**, *117*, 11499−11508.

(25) (a) DiPasquale, A. G.; Mayer, J. M. *J. Am. Chem. Soc.* **2008**, *130*, 1812−1813. (b) Coutsolelos, A.; Guilard, R.; Bayeul, D.; Lecomte, C. *Polyhedron* **1986**, *5*, 1157−164.

(26) Mahammed, A.; Giladi, I.; Goldberg, I.; Gross, Z. *Chem.—Eur. J.* **2001**, *7*, 4259−4265.

(27) Murakami, Y.; Yamada, S.; Matsuda, Y.; Sakata, K. *Bull. Chem. Soc. Jpn.* **1978**, *51*, 123−129.

(28) Nyokong, T.; Isago, H. *J. Porphyrins Phthalocyanines* **2004**, *8*, 1083−1090.

(29) Taube, H. *Chem. Rev.* **1952**, *50*, 69−126.

(30) Thomson, A. J.; Gadsby, P. M. A. *Dalton Trans.* **1990**, 1921−1928. (b) Yamamoto, T.; Nozawa, T.; Kobayashi, N.; Hatano, M. *Bull. Chem. Soc. Jpn.* **1982**, *55*, 3059−3063. (c) Kobayashi, N.; Nozawa, T.; Hatano, M. *Bull. Chem. Soc. Jpn.* **1981**, *54*, 919−924.

(31) (a) Lei, H.; Han, A.; Li, F.; Zhang, M.; Han, Y.; Du, P.; Lai, W.; Cao, R. *Phys. Chem. Chem. Phys.* **2014**, *16*, 1883−1893. (b) Nardis, S.; Cicero, D. O.; Licoccia, S.; Pomarico, G.; Berionni Berna, B.; Sette, M.; Ricciardi, G.; Rosa, A.; Fronczek, F. R.; Smith, K. M.; Paolesse, R. *Inorg. Chem.* **2014**, *53*, 4215−4227. (c) Conradie, J.; Ghosh, A. *Inorg. Chem.* **2011**, *50*, 4223−4225.

(32) (a) Ghosh, A.; Wondimagegn, T.; Parusel, A. B. J. *J. Am. Chem. Soc.* **2000**, *122*, 5100−5104. (b) Bendix, J.; Dmochowski, I. J.; Gray, H. B.; Mahammed, A.; Simkhovich, L.; Gross, Z. *Angew. Chem., Int. Ed.* **2000**, *39*, 4048−4051.

(33) (a) Rovira, C.; Kunc, K.; Hutter, J.; Parrinello, M. *Inorg. Chem.* **2001**, *40*, 11−17.

(34) (a) Hocking, R. K.; DeBeer George, S.; Gross, Z.; Walker, F. A.; Hodgson, K. O.; Hedman, B.; Solomon, E. I. *Inorg. Chem.* **2009**, *48*, 1678−1688. (b) Ye, S.; Tuttle, T.; Bill, E.; Simkhovich, L.; Gross, Z.; Thiel, W.; Neese, F. *Chem.—Eur. J.* **2008**, *14*, 10839−10851.

(35) (a) Vale, L. S. H. P.; Barata, J. F. B.; Santos, C. I. M.; Neves, M. G. P. M. S.; Faustino, M. A. F.; Tomé, A. C.; Silva, A. M. S.; Paz, F. A. A.; Cavaleiro, J. A. S. *J. Porphyrins Phthalocyanines* **2009**, *13*, 358−368. (b) Simkhovich, L.; Goldberg, I.; Gross, Z. *Inorg. Chem.* **2002**, *41*, 5433−5439.

DOI: 10.1021/ic502946t
Inorg. Chem. 2015, 54, 4652−4662